AlGaN/AlN integrated photonics platform for the ultraviolet and visible spectral range

MOHAMMAD SOLTANI,[1,*] **RICHARD SOREF,**[2] **TOMAS PALACIOS,**[3] **AND DIRK ENGLUND**[3]

[1]*Raytheon BBN Technologies, Cambridge, MA 02138, USA*
[2]*Department of Engineering, University of Massachusetts at Boston, Boston, MA, 02125, USA*
[3]*Department of Electrical Engineering and Computer Science, Massachusetts Institute of Technology, Cambridge, MA 02139, USA*
[*]*msoltani@bbn.com*

Abstract: We analyze a photonic integrated circuit (PIC) platform comprised of a crystalline $Al_xGa_{1-x}N$ optical guiding layer on an AlN substrate for the ultraviolet to visible (UV-vis) wavelength range. An Al composition of x~0.65 provides a refractive index difference of ~0.1 between $Al_xGa_{1-x}N$ and AlN, and a small lattice mismatch (< 1%) that minimizes crystal dislocations at the $Al_xGa_{1-x}N$/AlN interface. This small refractive index difference is beneficial at shorter wavelengths to avoid extra-small waveguide dimensions. The platform enables compact waveguides and bends with high field confinement in the wavelength range from 700 nm down to 300 nm (and potentially lower) with waveguide cross-section dimensions comparable to those used for telecom PICs such as silicon and silicon nitride waveguides, allowing for well-established optical lithography. This platform can potentially enable cost-effective, manufacturable, monolithic UV-vis photonic integrated circuits.

References and links

1. K. Takahashi, A. Yoshikawa, and A. Sandhu, *Wide Bandgap Semiconductors, Fundamental Properties and Modern Photonic and Electronic Devices* (Springer-Verlag, 2007).
2. S. Nakamura, S. Pearton, and G. Fasol, *The Blue Laser Diode: The Complete Strory* (Springer-Verlag, 2013).
3. T. Wunderer, C. L. Chua, J. E. Northrop, Z. Yang, N. M. Johnson, M. Kneissl, G. A. Garrett, H. Shen, B. Wraback, B. Moody, H. S. Craft, R. Schlesser, R. F. Dalmau, and Z. Sitar, "Optically pumped UV lasers grown on bulk AlN substrates," Phys. Status Solidi. **9**, 1–4 (2012).
4. M. Asif Khan, M. Shatalov, H. P. Maruska, H. M. Wang, and E. Koukstis, "III-nitride UV devices," Jpn. J. Appl. Phys. **44**(10), 7191–7206 (2005).
5. N. Tansu, H. Zhao, G. Liu, X. H. Li, J. Zhang, H. Tong, and Y. K. Ee, "III-nitride photonics," IEEE Photonics J. **2**(2), 241–248 (2010).
6. K. H. Li, X. Liu, Q. Wang, S. Zhao, and Z. Mi, "Ultralow-threshold electrically injected AlGaN nanowire ultraviolet lasers on Si operating at low temperature," Nat. Nanotechnol. **10**(2), 140–144 (2015).
7. M. Kneissl, T. Kolbe, C. Chua, V. Kueller, N. Lobo, J. Stellmach, A. Knauer, H. Rodriguez, S. Einfeldt, Z. Yang, N. M. Johnson, and M. Weyers, "Advances in group III-Nitride-based deep UV light-emitting diode technology," Semicond. Sci. Technol. **26**(1), 014036 (2011).
8. H. Hirayama, N. Maeda, S. Fujikawa, S. Toyoda, and N. Kamata, "Recent progress and future prospects of AlGaN-based high-efficiency deep-ultraviolet light-emitting diodes," Jpn. J. Appl. Phys. **53**(10), 100209 (2014).
9. C. Xiong, W. H. P. Pernice, and H. X. Tang, "Low-loss, silicon integrated, aluminum nitride photonic circuits and their use for electro-optic signal processing," Nano Lett. **12**(7), 3562–3568 (2012).
10. B. J. M. Hausmann, I. Bulu, V. Venkataraman, P. Deotare, and M. Loncar, "Diamond nonlinear photonics," Nat. Photonics **8**(5), 369–374 (2014).
11. N. Watanabe, T. Kimoto, and J. Suda, "The temperature dependence of the refractive indices of GaN and AlN from room temperatures up to 515° C," J. Appl. Phys. **104**(10), 106101 (2008).
12. A. W. Bruch, C. Xiong, B. Leung, M. Poot, J. Han, and H. X. Tang, "Broadband nanophotonic waveguides and resonators based on epitaxial GaN thin films," Appl. Phys. Lett. **107**(14), 141113 (2015).
13. R. Hui, Y. Wan, J. Li, S. Jin, J. Lin, and H. Jiang, "III-nitride-based planar lightwave circuits for long wavelength optical communications," IEEE J. Quantum Electron. **41**(1), 100–110 (2005).
14. H. Jung, C. Xiong, K. Y. Fong, X. Zhang, and H. X. Tang, "Optical frequency comb generation from aluminum nitride microring resonator," Opt. Lett. **38**(15), 2810–2813 (2013).

15. X. Guo, C. Zou, C. Schuck, H. Jung, R. Cheng, and H. X. Tang, "Parametric down-conversion photon pair source on a nanophotonic chip," arxiv: 1603.03726v1 (2016).
16. M. Rigler, J. Buh, M. P. Huffman, R. Kirste, M. Bobea, S. Mita, M. D. Gerhold, R. Collazo, Z. Sitar, and M. Zgonik, "Optical characterization of Al- and N-polar AlN waveguides for integrated optics," Appl. Phys. Express **8**(4), 042603 (2015).
17. C. Xiong, W. Pernice, K. K. Ryu, C. Schuck, K. Y. Fong, T. Palacios, and H. X. Tang, "Integrated GaN photonic circuits on silicon (100) for second harmonic generation," Opt. Express **19**(11), 10462–10470 (2011).
18. U. Dharanipathy, N. Vico Triviño, C. Yan, Z. Diao, J. F. Carlin, N. Grandjean, and R. Houdré, "Near-infrared characterization of gallium nitride photonic-crystal waveguides and cavities," Opt. Lett. **37**(22), 4588–4590 (2012).
19. A. E. Lim, J. Song, Q. Fang, C. Li, X. Tu, N. Duan, K. K. Chen, R. P. Tern, and T. Liow, ""Review of silicon photonic foundry efforts," IEEE J. Sel," IEEE J. Top. Quantum Electron. **20**, 8300112 (2014).
20. M. Poot, C. Schuck, X. S. Ma, X. Guo, and H. X. Tang, "Design and characterization of integrated components for SiN photonic quantum circuits," Opt. Express **24**(7), 6843–6860 (2016).
21. M. Soltani and R. Soref, "Free-carrier electrorefraction and electroabsorption in wurtzite GaN," Opt. Express **23**(19), 24984–24990 (2015).
22. C. Kao, A. Bhattacharyya, C. Thomidis, A. Moldawer, R. Paiella, and T. D. Moustakas, "A comparative study of UV electroabsorption modulators on bulk III-nitride films and multiple quantum wells," Phys. Status Solidi., C Curr. Top. Solid State Phys. **9**(3-4), 770–773 (2012).
23. M. Bickermann, B. M. Epelbaum, O. Filip, P. Heimann, S. Nagata, and A. Winnacker, "UV transparent single-crystalline bulk AlN substrates," Phys. Status Solidi **7**(c), 21–24 (2010).
24. See: www.hexatech.com
25. R. Dalmau, B. Moody, R. Schlesser, S. Mita, J. Xie, M. Feneberg, B. Neuschl, K. Thonke, R. Collaze, A. Rice, J. Tweedie, and Z. Sitar, "Growth and characterization of AlN and AlGaN epitaxial films on AlN single crystal substrates," J. Electrochem. Soc. **158**(5), H530–H535 (2011).
26. D. Zhu, D. J. Wallis, and C. J. Humphreys, "Prospects of III-nitride optoelectronics grown on Si," Rep. Prog. Phys. **76**(10), 106501 (2013).
27. Y. Jianchang, W. Junxi, L. Naixin, L. Zhe, R. Jun, and L. Jinmin, "High quality AlGaN grown on a high temperature AlN template by MOCVD," J. Semiconductors **30**(10), 103001 (2010).
28. G. Webb-Wood, Ü. Özgür, H. O. Everitt, F. Yun, and H. Morkoc, "Measurement of $Al_xGa_{1-x}N$ refractive indices," Phys. Status Solidi **188**, 793–797 (2001).
29. N. A. Sanford, L. H. Robins, A. V. Davydov, A. Shapiro, D. V. Tsvetkov, A. V. Dmitriev, S. Keller, U. K. Mishra, and S. P. DenBaars, "Refractive index study of $Al_xGa_{1-x}N$ films grown on sapphire substrates," J. Appl. Phys. **94**(5), 2980–2991 (2003).
30. N. Antoine-Vincent, F. Natali, M. Mihailovic, A. Vasson, J. Leymarie, P. Disseix, D. Byrne, F. Semond, and J. Massies, "Determination of the refractive indices of AlN, GaN, and $Al_xGa_{1-x}N$ grown on (111) Si substrate," J. Appl. Phys. **93**(9), 5223–5226 (2003).

1. Introduction

Numerous applications stand to benefit from photonic integrated circuits (PICs) in the UV and visible (UV-vis) spectrum, including biochemical sensing, UV-Raman spectroscopy, beam steering, nonlinear optics, and quantum photonics. A PIC platform for this wavelength range requires wide bandgap materials to be optically transparent, and preferably crystalline to avoid excess optical absorption and unwanted autofluorescence at shorter wavelengths. In this context, crystalline III-Nitride semiconductors, with their wide bandgap and unique optical properties, are now reaching a degree of maturity to enable versatile PICs with the possible integration of laser sources and detectors [1–8] operating down to the UV spectrum.

Here, we analyze how the crystalline AlGaN-on-AlN material platform could be leveraged for UV-vis PICs. For this study we limit the UV wavelength to 300 nm for which experimental data of the refractive index of $Al_xGa_{1-x}N$ is available, noting that in principle the platform has the potential to operate even down to ~250 nm wavelength for higher x in $Al_xGa_{1-x}N$. We consider a substrate consisting of a bulk c-wurtzite AlN wafer or a thick AlN epitaxial buffer on silicon, silicon carbide, or sapphire, and an AlGaN waveguide layer. The architectures uses the same AlN platform for both AlGaN electronics and PICs. Table 1 summarizes the properties of AlN and GaN compared to other wide bandgap integrated photonic materials. Figure 1 shows a range of applications that can benefit from a UV-vis PIC platform.

A variety of III-Nitride waveguide structures have been studied for the visible/infrared spectra. A common structure consists of an epitaxial GaN waveguide grown on sapphire first

developed for GaN lasers [2] and later extended to infrared applications [12]. The large lattice mismatch (14%) and temperature expansion coefficient mismatch between GaN and sapphire results in large crystalline dislocation density for GaN which can contribute to optical loss. Another structure consists of a GaN waveguiding layer on a thick AlGaN cladding epitaxially grown on a substrate such as GaN or sapphire [13]. Because of the 365 nm bandgap of GaN, this platform does not extend to the UV. In addition, the AlGaN cladding layer needs to be thick (> 3 μm) to avoid leakage radiation to the underneath GaN substrate for visible wavelengths.

Table 1. Comparison of AlN and GaN with other UV bandgap integrated photonic materials*

	Diamond	GaN	AlN	SiO_2	Si_3N_4
refractive index @ λ = 500 nm	2.4	2.42	2.13	1.45	2.04
bandgap (nm)**	230	365	200	140	250
crystalline	yes	yes	yes	no	no
electro-optic coeff. (pm/V)	NA	~1	~1	NA	NA
thermo-optic coeff. (K^{-1})	10^{-6}	1.6×10^{-4}	3.6×10^{-5}	10^{-5}	2.5×10^{-5}
thermal conductivity ($W.m^{-1}.K^{-1}$)	2200	130	285	1.4	30
active integratioon	no	yes	yes	no	no

*: The data in this table are available in many references including Refs [1,9–11] cited here.

**: Above the bandgap wavelength, the material starts to become transparent.
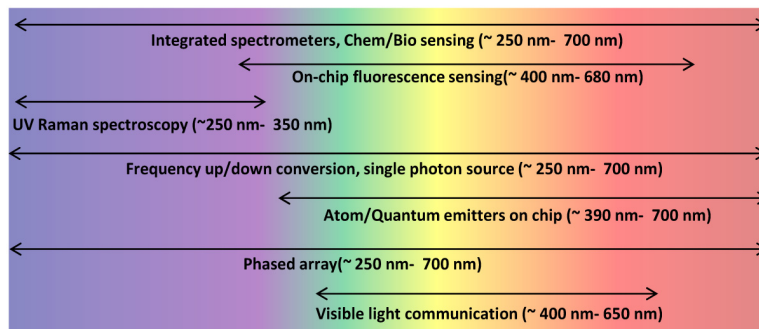

Fig. 1. Example of target applications benefiting from UV-visible integrated photonics.

There has been extensive work using sputtered AlN as the waveguide [9,14,15] on a SiO_2 cladding residing on silicon with promising low-loss results in the infrared (~1550 nm) [14] and a further excess loss at near-infrared (~780 nm) [15]. Since this AlN is amorphous, the waveguide is expected to show larger optical loss and unwanted autofluorescence at shorter wavelengths. Also, the large refractive index contrast between AlN and SiO_2 results in small cross-sectional dimensions (e.g. ~100 nm at λ~300 nm) for single mode ridge waveguides, making their lithography difficult and exacerbating optical scattering losses. A recent work shows epitaxially grown AlN-on-sapphire waveguides [16]. Such waveguides suffer from a large lattice mismatch between AlN and sapphire (~13%) as well as large refractive index difference (~0.5). Other approaches include bonding of GaN to SiO_2 [17], as well as free-standing GaN membrane waveguides [18]. Another promising wide bandgap photonic platform that has been pursued is crystalline diamond on SiO_2 [10]. In this platform, diamond lacks active integration and efficient tuning capabilities (see Table 1), and its large refractive index contrast to that of SiO_2 makes waveguide dimensions very small in the UV.

In the $Al_xGa_{1-x}N$-on-AlN architecture considered here, an x~0.65 provides a sufficiently high index contrast (~0.1), transparency down to ~260 nm, small lattice mismatch ~1% with

potentially manageable low strain at the AlGaN/AlN interface, and single-mode waveguides with easy-to-fabricate dimensions comparable to telecom PICs made of silicon and silicon nitride [19,20]. The AlGaN waveguides can have cross-sectional dimensions of multiple wavelengths. This reduces the interaction of the optical mode with the waveguide sidewalls, and thereby can greatly reduce scattering loss from waveguide sidewalls. Moreover, the large mode-field diameter in the AlGaN waveguide is convenient for waveguide edge-coupling.

The paper is organized as follows. Section 2 presents the AlGaN waveguide structure and its refractive index contrast with respect to AlN. Sections 3 and 4 analyze the mode properties of AlGaN waveguides and bends, respectively; Section 5 discusses AlN as a substrate for a wafer scale photonic platform and its challenges; and Section 6 summarizes.

2. Waveguiding structure and refractive index of $Al_xGa_{1-x}N$

Consider the ridge waveguiding structure shown in Fig. 2(a). The waveguide consists of an $Al_xGa_{1-x}N$ ridge on a pedestal of AlN of height h on the AlN substrate. This pedestal reduces bending losses (see Sect. 4). The overcladding material, depending on the application, can be air or any other wide bandgap and transparent material such as water or SiO_2 that have a refractive index lower than that of AlGaN. The $Al_xGa_{1-x}N$ alloy has a bandgap from ~3.42 eV (~365 nm) for x = 0 to ~6.2 eV (~200 nm) for x = 1. To keep the lattice mismatch at the AlGaN/AlN interface below 1% and attain a large UV bandgap, we assume x$\geq$0.65 as indicated in the pink region in Fig. 2(b). Though increasing the x reduces the refractive index difference between $Al_xGa_{1-x}N$ and AlN, we will show that adequate optical mode confinement is available for the waveguides.
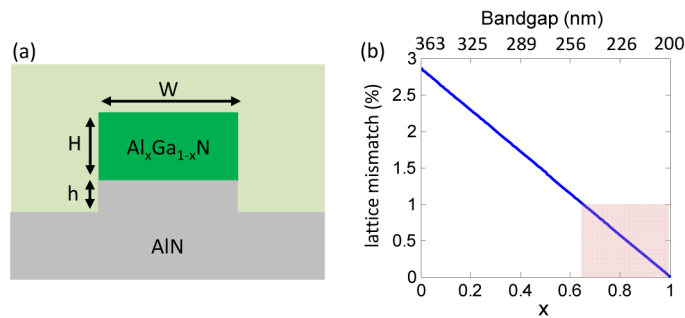

Fig. 2. (a) cross section of the $Al_xGa_{1-x}N$ waveguide discussed here. (b) Variation of $Al_xGa_{1-x}N$/AlN lattice-mismatch vs. x. The top horizontal axis shows the bandgap of $Al_xGa_{1-x}N$ in the wavelength unit for the each x value.
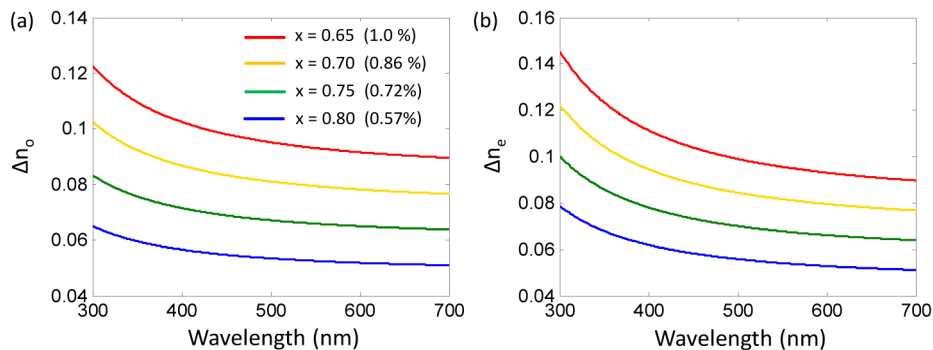

Fig. 3. Plots of the refractive index difference between the $Al_xGa_{1-x}N$ and AlN for (a) ordinary and (b) extraordinary indices with the x values and lattice mismatches shown in the inset of (a).

Figures 3(a) and 3(b) show the refractive index difference for both ordinary (Δn_o) and extraordinary (Δn_e) directions between the $Al_xGa_{1-x}N$ and AlN at four values of x>0.65 (see Appendix section on the refractive index of AlGaN). For x = 0.65, Δn_o ~0.090-0.12 and Δn_e ~0.090-0.14 over a wavelength range of 300 nm – 700 nm. The values of Δn_o and Δn_e will approximately determine the guided-mode confinement for the transverse-electric (TE) and transverse-magnetic (TM) polarization modes, respectively.

3. Results of photonic waveguide analysis

For the simulation of the modes of the waveguide shown in Fig. 2(a) we choose the popular aspect ratio of W = 2.5 H and consider two cases of h = 0 and h = H/2. We choose SiO_2 as the overcladding for the simulation. The results would not change much if we had selected air or water overcladding because the refractive index of these three materials are much smaller than that of AlGaN, and so the waveguiding condition is mainly governed by the AlGaN/AlN refractive index difference.

Figures 4(a) and 4(b) show a map of the simulated TE and TM modes for an $Al_{0.65}Ga_{0.35}N$ waveguide. A broad optical spectrum from 300 to 700 nm is guided by varying the waveguide W and H. The regions of single-mode, multi-mode, and mode cut-off are given in Fig. 4(a) and 4(b). The colormaps represent the power confinement factor in the core of the waveguide. From these figures we see that single mode propagation and strong mode confinement are possible for Δn ~0.1 (for x = 0.65, see Fig. 3). The TE polarization [Fig. 4(a)] is guided over a narrower wavelength range than the TM polarization [Fig. 4(b)] because of a smaller in-plane refractive index difference Δn_o than the out-of-plane refractive index difference Δn_e. The insets in Fig. 4(a) and 4(b) show the optical power-density mode profiles, corresponding to the point marked by the star in Fig. 4(a) and 4(b).
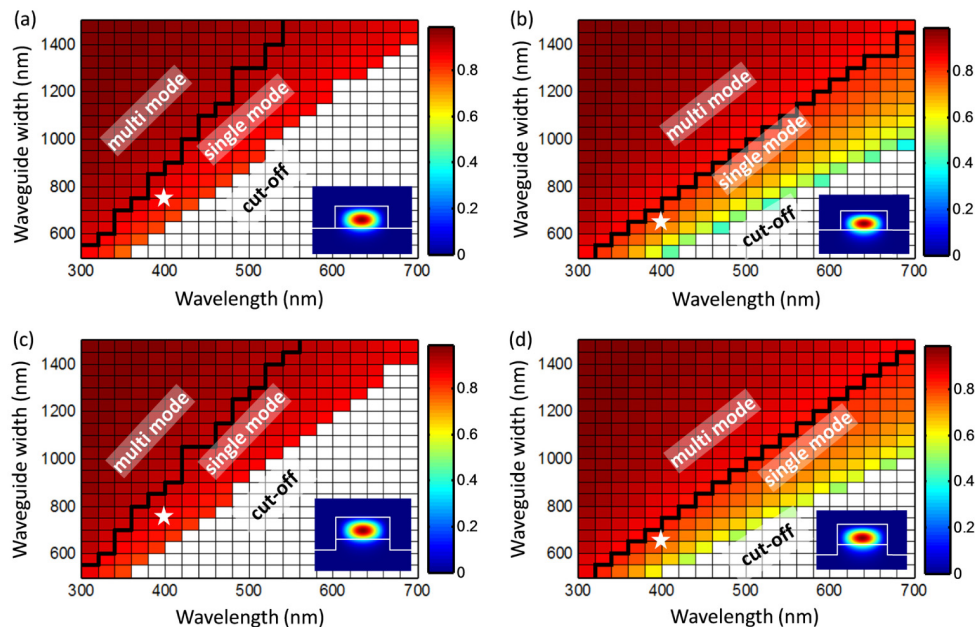

Fig. 4. Simulated guided-mode map for an $Al_{0.65}Ga_{0.35}N$ waveguide with the general structure shown in Fig. 2(a) when W = 2.5 H and for the following cases: (a) TE polarization, h = 0, (b) TM polarization, h = 0, (c) TE polarization, h = H/2, (d) TM polarization, h = H/2. In each figure, the colormap represents the power confinement factor in the core of the waveguide. The regions of single-mode, multi-mode, and cut-off have been highlighted. The colorbars for each figure correspond to the colormap data. The insets in a-d show the waveguide mode intensity profile corresponding to the white star marker in the guided-mode map.

We repeat the waveguide analysis for a finite-thickness pedestal (h>0). Figures 4(c) and 4(d) again show broadband waveguiding, for the TE and TM polarizations, respectively and for h = H/2. The guided modes are similar for h = 0 and h = H/2 as seen from the results in Fig. 4, but the finite pedestal thickness reduces radiation in waveguide bends, as discussed in Section 4.

We repeat these simulations for $Al_{0.75}Ga_{0.25}N$ waveguides under the TE and TM, W = 2.5H, and h = 0 or H/2 constraints (not shown). Simulations for x = 0.65 and x = 0.75 provide a straight-line approximation to the single-mode condition as W = $\alpha\lambda + \beta$ (where λ is the wavelength and α and β are constants) that allows direct comparison of W(single-mode) vs. λ. Figure 5 plots these lines that delineate single-mode conditions of AlGaN waveguides in the UV-vis range.
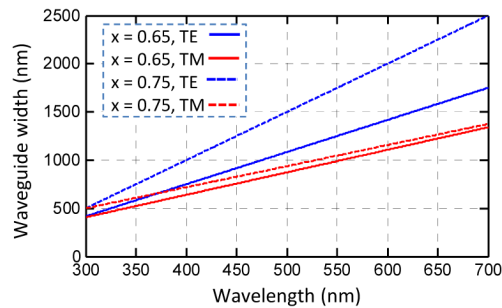

Fig. 5. A straight line approximation showing the single-mode condition for TE and TM polarization modes of an $Al_xGa_{1-x}N$ waveguide for x = 0.65 and 0.75, and for the case of h = 0, and W = 2.5 H. The single-mode condition in these plots corresponds to a mode confinement factor close or above 80%. The h = H/2 results are not shown as they are close to those of h = 0.

To show that a small refractive index difference between AlGaN and AlN is very beneficial for waveguide design at shorter wavelength, we simulated the guided modes at a UV wavelength of 300 nm for various waveguide heights (H) and widths (W). Figure 6(a) and 6(b) show the results for the TE and TM polarizations respectively. From these results and for a single mode condition, the waveguide dimension are comparable to those used for Si waveguide at telecom wavelengths, thereby, the lithography of these UV waveguides is possible with existing photolithography technology.
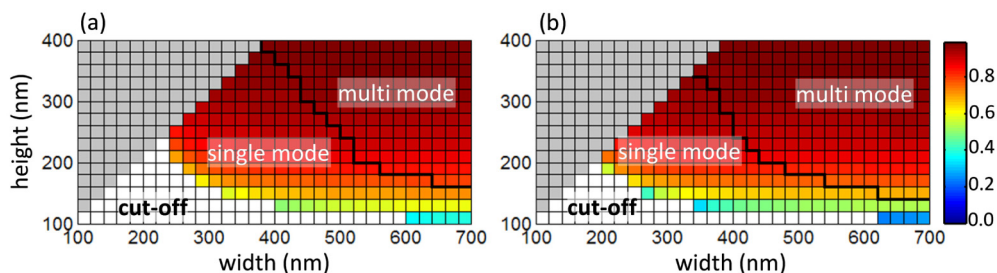

Fig. 6. Simulated guided-mode map for an $Al_{0.65}Ga_{0.35}N$ waveguide for different heights (H) and widths (W) and a pedestal h = 0, at a wavelength of 300 nm for (a) TE and (b) TM polarizations. The colormap represents the power confinement factor in the core of the waveguide. The regions of single-mode, multi-mode, and cut-off have been highlighted. For each waveguide height, the waveguide width varies from that height value to 700 nm; therefore, the gray region is excluded in our analysis.

The passive waveguides considered thus far could be modified for electro-optical modulation through the Pockels effect or carrier injection/depletion [21]. The Pockels coefficient of AlGaN is expected to be close to that of AlN (~1 pm/V [9]), though it may be

increased by strain engineering. A reverse-biased PIN diode across intrinsic AlGaN would induce Franz-Keldysh electro-absorption modulation at photon energies ~50 meV below the band edge [22].

4. Analysis of the bend loss

To analyze bending losses, we simulate optical resonances of circular $Al_{0.65}Ga_{0.35}N$ microring resonators on an AlN substrate and find their radiation-limited quality factor (Q_r). The simulations are for TE-like modes near a wavelength of 300 nm. We find Q_r using the relation $Q_r = \omega_r/(2\omega_i)$ where ω_r and ω_i are the real and imaginary part of the resonance, respecetively.

Figure 7(a) plots the simulated Q_r for two pedestal thicknesses of h = 0 and h = H/2. The results in Fig. 7(a) show that compact resonators with high Q factors can be obtained for a small refractive index difference between $Al_{0.65}Ga_{0.35}N$ and AlN (see Fig. 3 for the refractive index data). For h = H/2, Q_r is consistently higher and permits high Q factors for radii below 5 μm. Figures 7(b) and 7(c) show the cross section mode profiles for the electric field in the radial direction for a radius of 15 microns and for two cases of h = H/2 and h = 0, respectively. Figure 7(d) shows the roundtrip bending loss of the resonators simulated in Fig. 7(a). The roundtrip loss in dB scale is $10\,log_{10}(e^{-\alpha 2\pi R})$ where R is the radius and α is the propagation loss per unit of length, and is related to Q_r as $\alpha = 2\pi n_g/(\lambda Q_r)$, where λ is the wavelength and n_g is the group index of the optical mode.

From the results in Fig. 7 we can conclude that compact and low loss bends can be designed. Although the resonator simulations in Fig. 7 are for an $Al_xGa_{1-x}N$ with x = 0.65, compact resonators can be still obtained by higher or lower x values (e.g. x = 0.7, or x = 0.6).
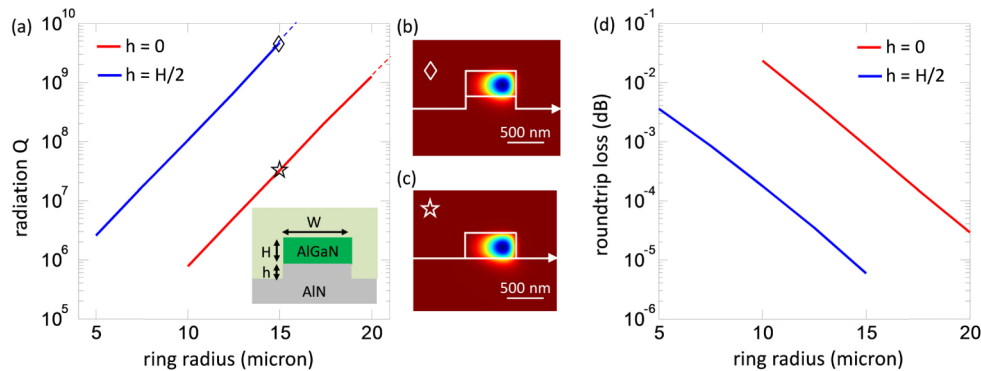

Fig. 7. (a) Simulated radiation Q for the TE mode of an $Al_{0.65}Ga_{0.35}N$ ring resonator vs. its radius for a resonance wavelength ~300 nm and for h = 0 and h = H/2. The inset shows the ring cross section. For this simulation W = 700 nm, H = 350 nm. (b)-(c) Cross section of the radial electric field mode profiles for a ring radius of 15 microns for h = H/2 and h = 0, respectively. (d) Roundtrip loss of the rings in (a).

5. AlN as a substrate

C-axis AlN wafers are cut from a wurtzite single-crystal AlN boule grown by proprietary methods [23–25], and their UV transparency depends upon the crystal quality. The largest AlN boules grown to date have 50 mm diameter, and 32 mm diameter is available commercially [24]. A current challenge is to reduce the crystalline dislocation density in AlN. State-of-the-art single crystal growth of AlN produces dislocation densities below $1000/cm^2$, and selected areas can have <100 defects/cm^2 [24]. In the present art, AlN wafers show an absorption of less than 15 cm^{-1} over the 230 to 700 nm wavelength range, and less than 8 cm^{-1} for the 510 to 700 nm wavelengths [23]. These optical absorption results are promising and can be further improved by advancing the crystal growth techniques. A possible approach

to further reduce dislocations near the AlGaN waveguide layer is to epitaxially grow a buffer layer of AlN on this AlN wafer before growing AlGaN.

A near-term approach for large-scale wafers of AlGaN films is to use substrates of SiC, Si [26], or sapphire [27] with an optically thick, epitaxially grown spacer layer of AlN. Figure 8(a) shows a waveguiding structure in this platform. The lattice mismatch between the AlN and these aforementioned substrates determines the dislocation density at the lower AlN surface. Figure 8(b) summarizes the lattice mismatch between AlN and the potential growth substrates. With recent advances in growth techniques [8], the growth of an AlN spacer layer with minimal dislocation density on these substrates is possible.

With a small lattice mismatch (<1%) between the AlN and AlGaN for the geometries studied here, reducing the crystalline dislocations of AlGaN is foreseeable by proper strain engineering. Recent works on the epitaxial growth of GaN on Sapphire with a lattice mismatch of ~14% show a dislocation density ~10^8/cm^2 (i.e. 1/µm^2) [12]. The defect density in the AlGaN-on-AlN architecture with <1% lattice mismatch should be much smaller, potentially allowing for zero dislocations across ring resonators with areas on the scale of tens of µm^2.
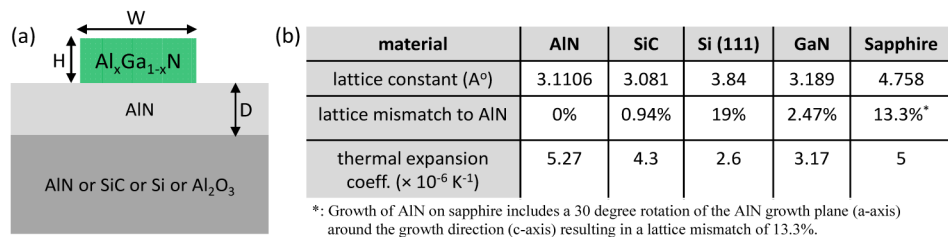

material	AlN	SiC	Si (111)	GaN	Sapphire
lattice constant (A^o)	3.1106	3.081	3.84	3.189	4.758
lattice mismatch to AlN	0%	0.94%	19%	2.47%	13.3%*
thermal expansion coeff. (× 10^{-6} K^{-1})	5.27	4.3	2.6	3.17	5

*: Growth of AlN on sapphire includes a 30 degree rotation of the AlN growth plane (a-axis) around the growth direction (c-axis) resulting in a lattice mismatch of 13.3%.

Fig. 8. (a) AlGaN-on-AlN waveguide structure on a substrate that can be AlN, SiC, Si or Al$_2$O$_3$. The thickness D is large enough (e.g. 2-3 µm) to avoid the leaking of the optical mode to the underneath substrate if not AlN. (b) Lattice parameters and temperature expansion of crystal wafers upon which AlN has been epitaxially grown.

6. Conclusions

Al$_x$Ga$_{1-x}$N-on-AlN is a promising platform for photonic integrated circuits for wavelengths 250nm-to-700nm in the UV-visible range. An Al content x~0.65 results in ~1% lattice mismatch at Al$_x$Ga$_{1-x}$N/AlN interface and a refractive index differences of ~0.1 between these two layers. The latter results in a large single-mode waveguide cross section of multiple wavelengths, relaxing lithographic tolerances and likely lowering scattering losses. In particular, we present single-mode waveguide designs for TE$_o$ and TM$_o$ modes for 300 - 700 nm wavelengths. We also show that the platform enables compact and high Q resonators, and correspondingly low loss bent waveguides. With a ~1% lattice mismatch between AlGaN and AlN we expect smaller dislocation densities, though the relationship between interface dislocations and optical losses is not presently clear and will need to be explored experimentally. The presented single-crystal UV-vis photonics platform would enable a range of applications including sensing to quantum information science and optical communications.

7. Appendix

Early works on the measurements of the refractive index of Al$_x$Ga$_{1-x}$N showed large discrepancy, though later measurements converged [11,28–30]. From our thorough investigation among the more recent works, we considered those of [28] and [29] as they measured both ordinary and extraordinary refractive indices of Al$_x$Ga$_{1-x}$N for high x values and their results were used or validated in later works [11]. While the data in [29] are for selected x values, the data in [28] cover the complete range from x = 0 (GaN) to x = 1 (AlN).

We estimated the ordinary and extraordinary refractive indices of $Al_xGa_{1-x}N$ from the Sellmeier expression in [28]:

$$n(\lambda)^2 = 1 + \frac{A_0 \lambda^2}{\lambda^2 - L_0^2}, \quad (A_0 = B_0 + B_1 x, \quad L_0(x) = C_0 + C_1 x + C_2 x^2), \quad (1)$$

where λ is the wavelength of light in nm. Table 2 shows the coefficients used in the above expressions ([28]). Since these coefficients had a large tolerance range, we adjusted them within their range by matching Eq. (1) with the refractive index results in [29].

Although the measurements in [28] and [29] started from a wavelength of ~ 440 nm, we have extended Eq. (1) to 300 nm, and to validate this, we compared Eq. (1) to [30] that measured the refractive index of AlGaN down to 300 nm. In [30] a net refractive index for AlGaN was reported as their apparatus did not distinguish between the ordinary and extraordinary indices. This comaprison showed similar dispersion behavior for the AlGaN refractive index. In addition, the refractive index difference between AlGaN and AlN is similar from Eq. (1) and [30] (for our guided-mode studies, the Δn is more relevant than the absolute values of indices).

Table 2. Coefficients used for the refractive index expression in Eq. (1) [28]. The numbers in the prantheses are the ones that we selected to match Eq. (1) with the the the data in [29].

Coefficient	Ordinary index (n_o)	Extraordinary index (n_e)
B_0	4.1446 $\pm$ 0.0146 (**4.1446**)	4.2957 $\pm$ 0.0165 (**4.2957**)
B_1	−1.0021 $\pm$ 0.0273 (**-1.0021**)	−0.9817 $\pm$ 0.0310 (**-0.9817**)
C_0	190.719 $\pm$ 2.48 (**190.719**)	191.71 $\pm$ 2.23 (**191.71**)
C_1	−82.999 $\pm$ 12.363 (**-75**)	−76.363 $\pm$ 11.142 (**-75**)
C_2	27.521 $\pm$ 11.619 (**37.521**)	23.427 $\pm$ 10.471 (**25**)